**Electronic Supplementary Information**

for

# Dynamics of Carbohydrate Strands in Water and Interactions with Clay Minerals: Influence of pH, Surface Chemistry, and Electrolytes

Tariq Jamil,[1] Jacob R. Gissinger,[2] Amanda Garley,[1] Nabanita Saikia,[1] Arun K. Upadhyay,[3]
Hendrik Heinz[1,2*]

[1] Department of Chemical and Biological Engineering, University of Colorado at Boulder, Boulder, CO 80309, USA

[2] Materials Science and Engineering Program, University of Colorado at Boulder, Boulder, CO 80309, USA

[3] The Procter & Gamble Company, Cincinnati, OH 45202, USA

**This PDF file includes:**

- Figures S1 to S9
- Tables S1 to S3
- Supplementary Text Sections S1 to S4
  - Derivation of All-Atom Models for Veegum Clay
  - The Shape of Clay Platelets
  - Details of Computational Methods
  - Details of Elemental Analysis
- Captions for Movies S1-S8

**Other Supplementary Materials for this manuscript include the following:**

- Movies S1 to S8
- Molecular Models and Force Field Files

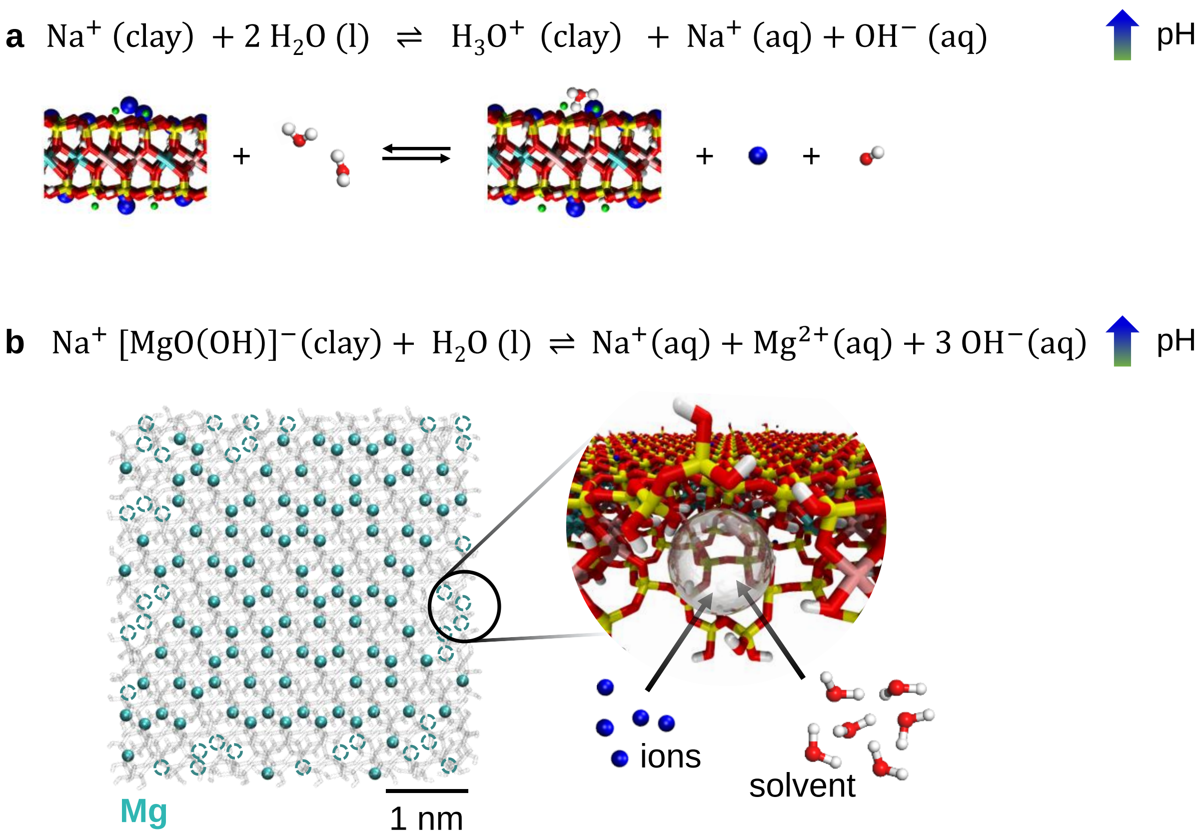

**Figure S1.** Veegum interactions with water increase the pH value of veegum dispersions to ~9 in a non-buffered solution. (a) Instant exchange of a small fraction of superficial sodium ions by hydronium ions raises the pH value to around 9. (b) Leaching of Mg atoms along the edge of the clay platelet can further increase the pH value over time. A model structure of degraded veegum clay with loss of magnesium in the octahedral sheet and a stoichiometric amount of $Na^+$ and $Ca^{2+}$ ions atop the surface is shown below. On the left, a top view of the inner octahedral sheet is shown and dashed circles indicate leached Mg atoms. The inset on the right shows the formation of void spaces in the inner part of the clay layer that results from Mg removal from the edge (transparent sphere). Solvent molecules and ions can enter into this space.

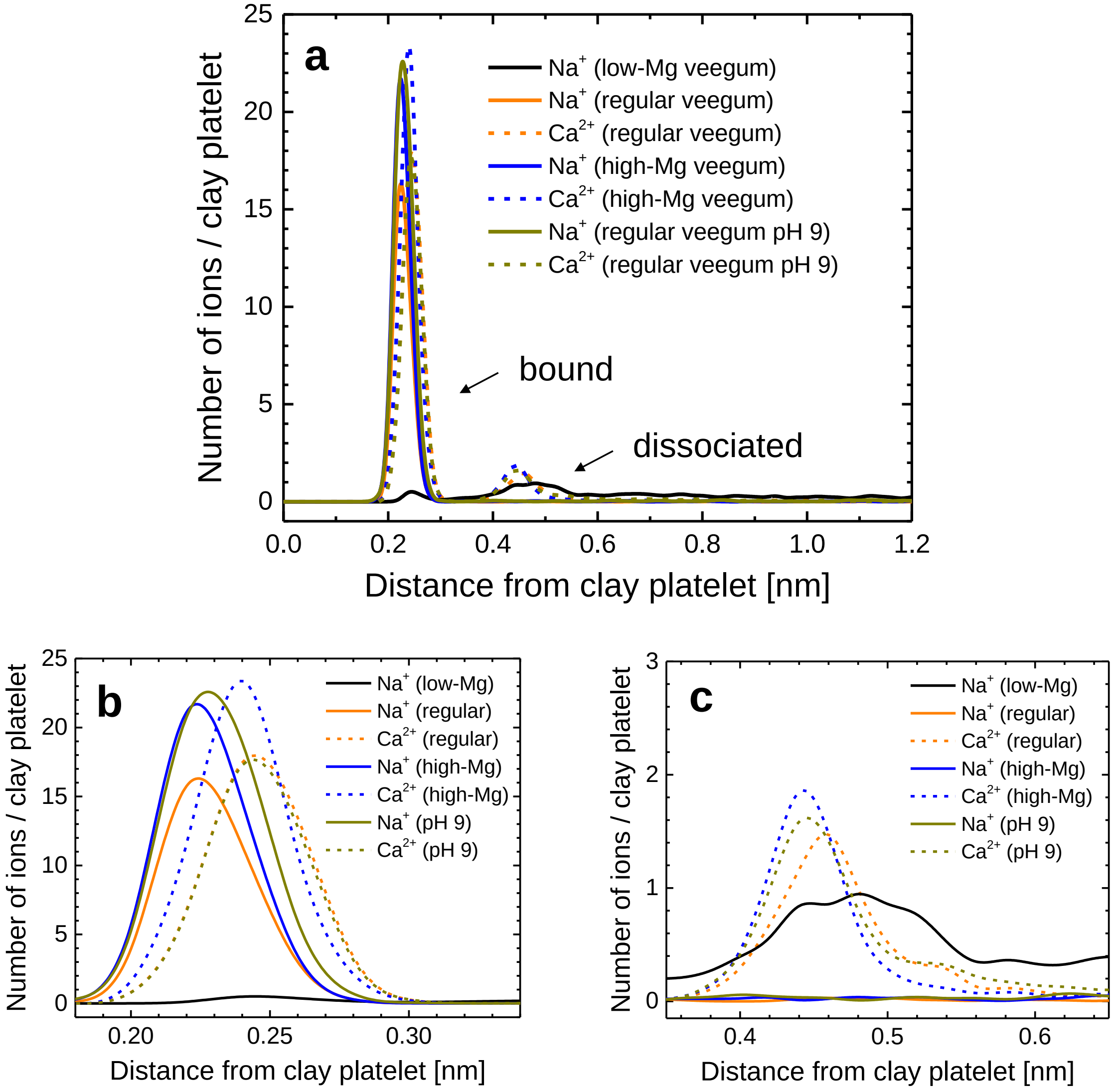

**Figure S2.** Density profile for $Na^+$ and $Ca^{2+}$ ions on the surface of veegum clay platelets in aqueous solution. (a) The total density profile shows that over 95% of sodium ions are dissociated in low Mg veegum (montmorillonite) and approximately 15-20% of sodium and calcium ions are dissociated in regular and high Mg veegum. Dissociation was defined as >3 Å distance from the surface atomic layer. The influence of pH value was moderate. Data are shown for pH ~3.5 with 0% ionization of silanol edge groups, and the data at pH ~9 with 50% ionization of silanol edge groups for regular veegum are similar. (b, c) Insets of (a) show details of the first and second layers of ions. Clay minerals with mixed monovalent and divalent ions, i.e., other than montmorillonite, show both ions in the first layer and only divalent ions in the second layer owed to the highly favorable hydration shells of $Ca^{2+}$ ions. The data are an average over all ions near the clay platelet, including atop the basal plane and near the edges. The distance of each ion from the nearest surface atom (Si, O, Al, Mg) was determined in 90 individual snapshots over 90 ns simulation time to compute the average distance profile over all ions and over all snapshots.

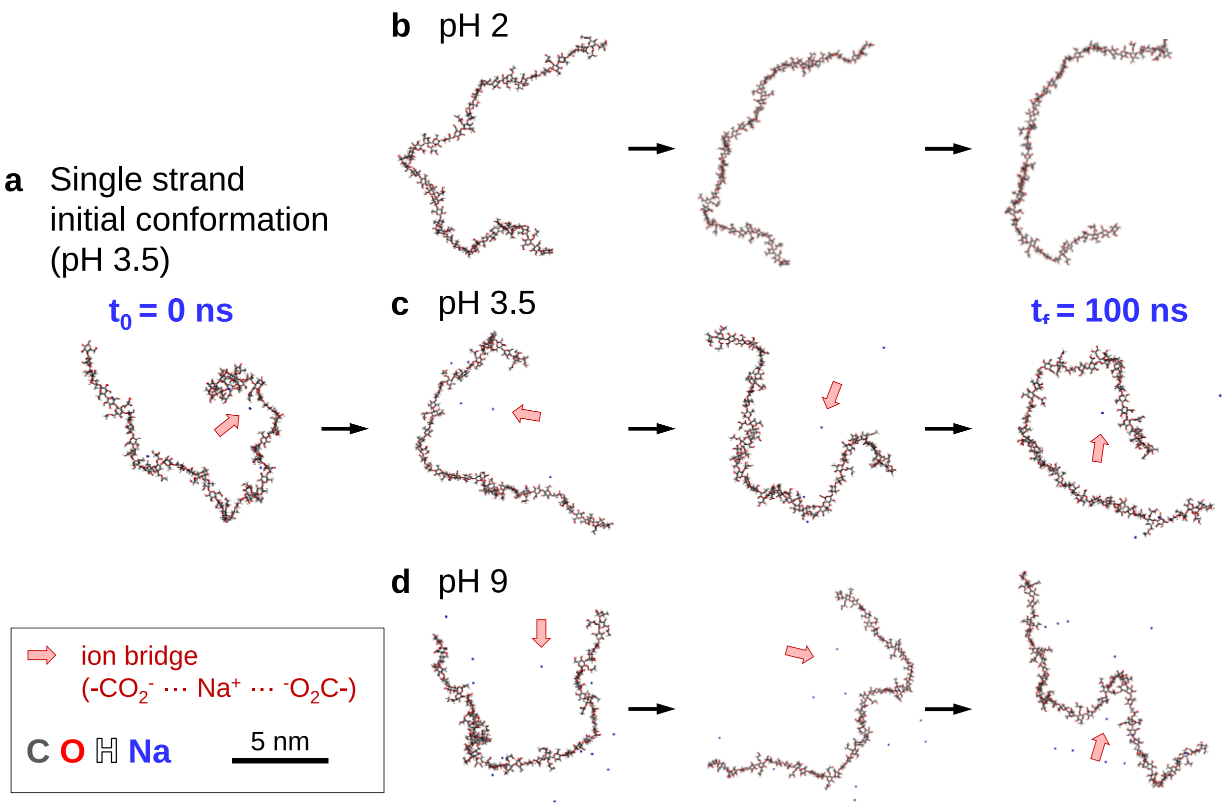

**Figure S3**. Conformation of single strands of gellan gum in dilute aqueous solution (~1.7 wt%). (a) Start conformation of a single-strand of gellan gum at pH 3.5. (b-d) Representative snapshots over a simulation time of 100 ns at pH values of 2, 3.5, and 9 (same as for pH > 5). At pH 2, conformational changes are slow and limited. At higher pH, the negatively charged backbone temporarily bends in response to the motion of the cations (arrows). Gellan gum changes conformations more frequently due to these intramolecular ion bridges.

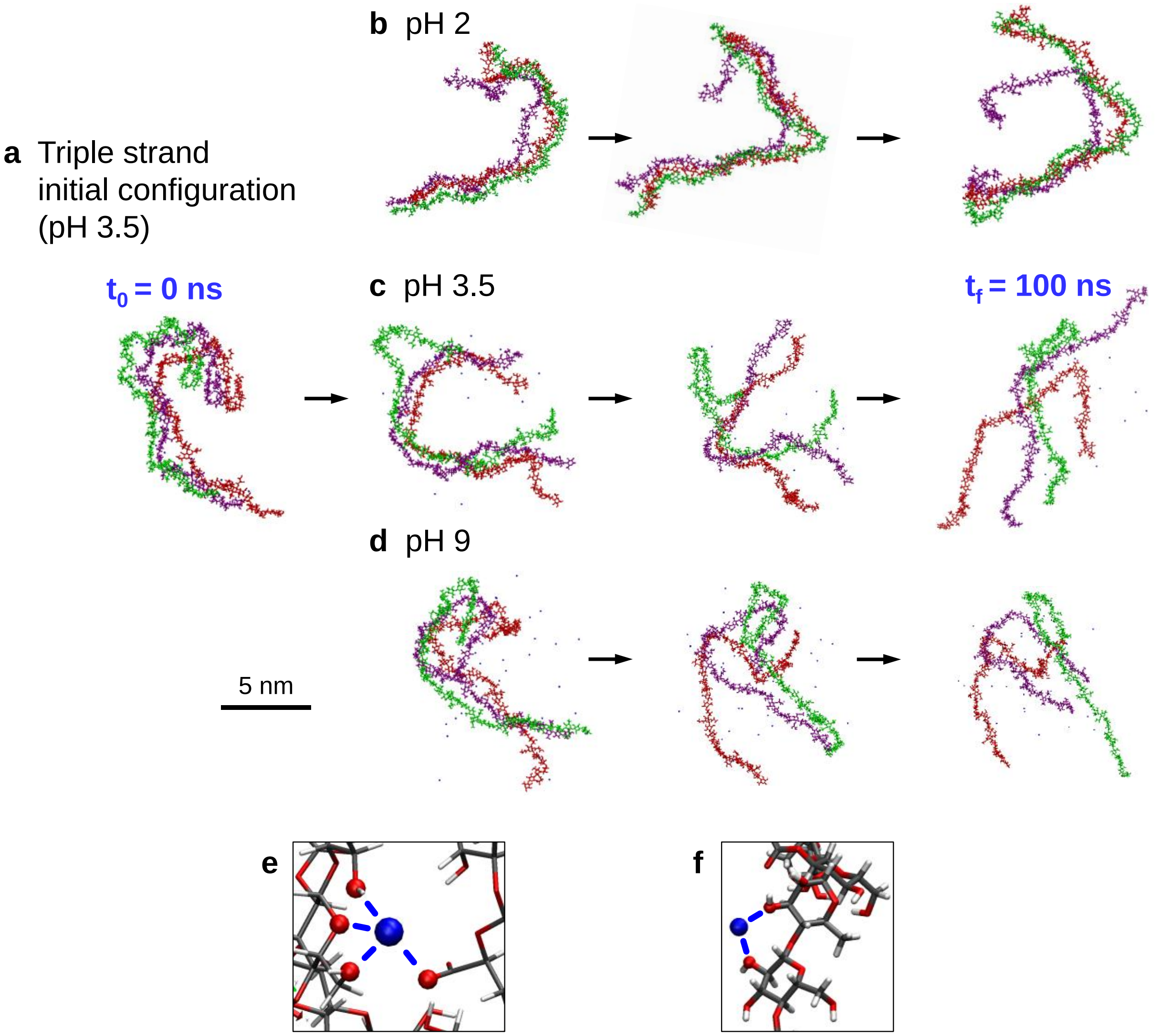

**Figure S4**. Conformation of triple-strands of gellan gum in aqueous solution (~5.0 wt%). (a) Start configuration for molecular dynamics simulations at pH = 3.5. (b-d) Representative snapshots over a simulation time of 100 ns for pH values of 2, 3.5, and 9 (same as for pH > 5). At pH = 2, the strands have no ionic groups, interact through multiple hydrogen bonds, and remain at close distance. At pH 3.5 and 9, the carbonic acid groups dissociate, the ions hydrate, and the strands separate. The high number of sodium ions induces more intramolecular and intermolecular ion bridges (far and close) compared to double strands. The high number of such interactions between different strands increases the overall attraction between strands compared to lower pH value. (e)

Coordination of a sodium ion by two strands of gellan gum. Oxygen atoms in two hydroxyl groups, in a carbohydrate ring, and in a carboxylate group of another strand (lower right), as well as water molecules (not shown) form the $Na^+$ coordination shell. (f) Intra-strand coordination of a $Na^+$ ion by two hydroxyl groups. Coordination by the ions accelerates conformational dynamics and tends to increase overall stiffness and end-to-end length.

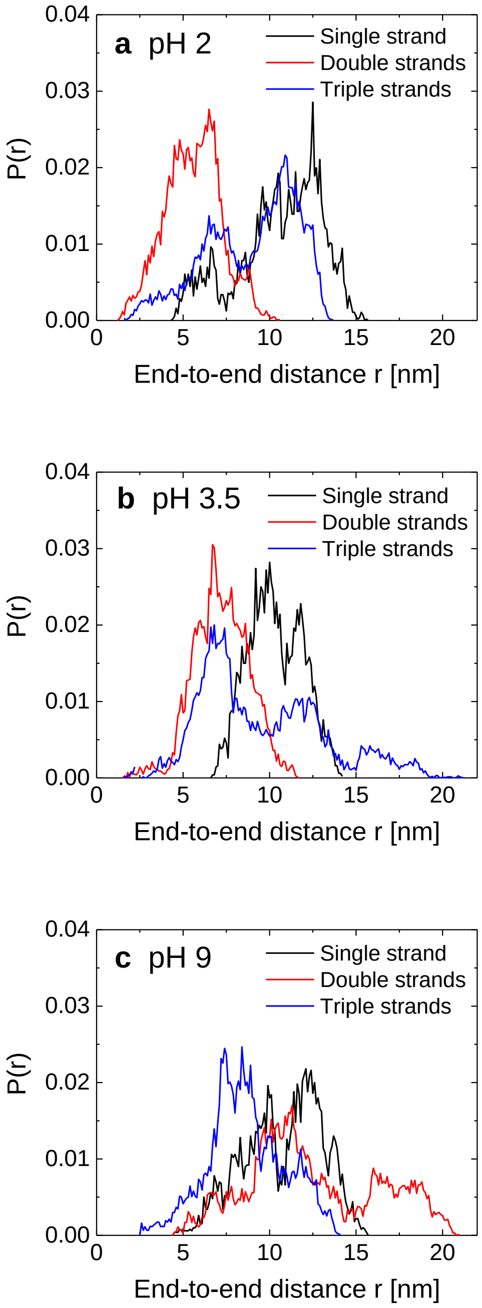

**Figure S5.** Distribution of root mean square end-to-end distances *r* for a 48-carbohydrate ring polymer of gellan gum in dilute aqueous solution. (a) pH 2. (b) pH 3.5. (c) pH 9. The cation cloud around the polymer at higher pH values tends to increase the average end-to-end length, the width and bimodal features of the distributions. At the same time, more frequent switching between folded and extended states occurs.

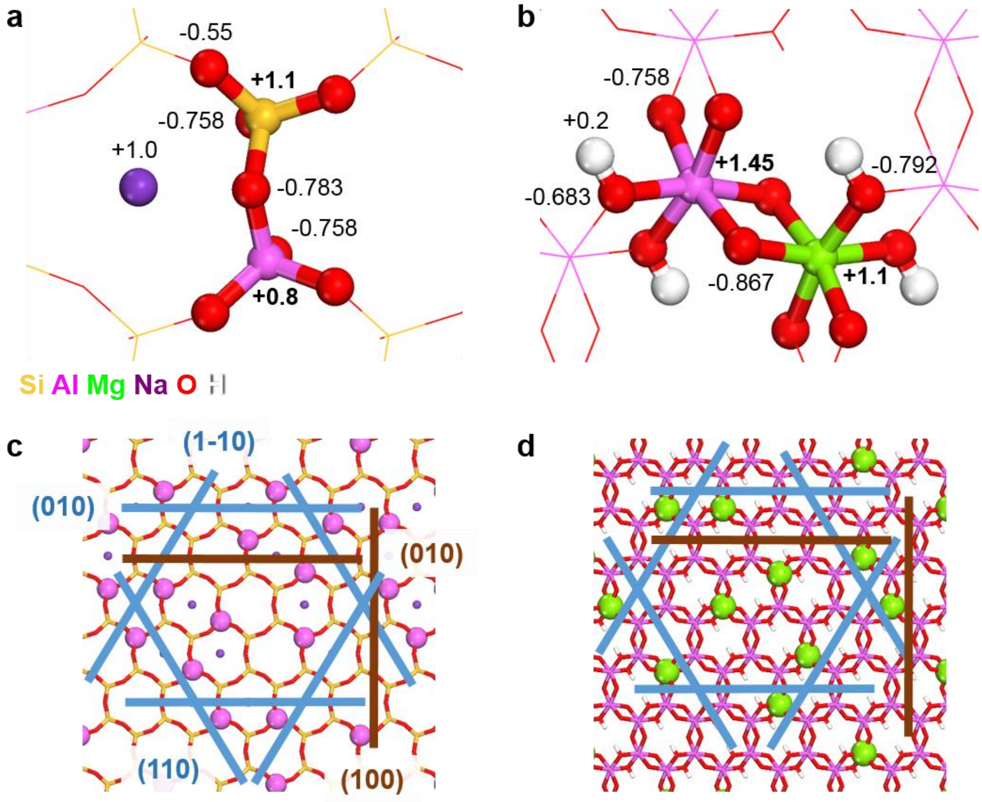

**Figure S6.** Bonding and cleavage planes in the tetrahedral silicate and octahedral aluminate layers (adapted from ref. [1]). (a) Local top view of the tetrahedral silicate layer, including atomic charges. (b) Local top view onto the octahedral aluminate layer, including atomic charges. (c, d) View of a larger area and indication of bond cleavage. Blue lines mark cleavage planes leading to pseudo-hexagonal shape, brown lines cleavage planes leading to square-like or rectangular shape. The number of Si-O-Si and Al-O-Al bonds cleaved per unit length is closely the same along the blue and brown planes. In (c), number counts are 4 to 5 Si-O-Si bonds per line. In (d), number counts are 10-12 Al-O-Al bonds per line. Linear bond densities are slightly lower along the blue lines than along the brown (100) line and the geometry along the blue lines may kinetically favor crystal growth along these planes. Minor differences in the linear density of bonds along the brown lines and other (hkl) cleavage planes lead to similar equilibrium cleavage energies so that grinding of clay particles leads to irregular shapes.

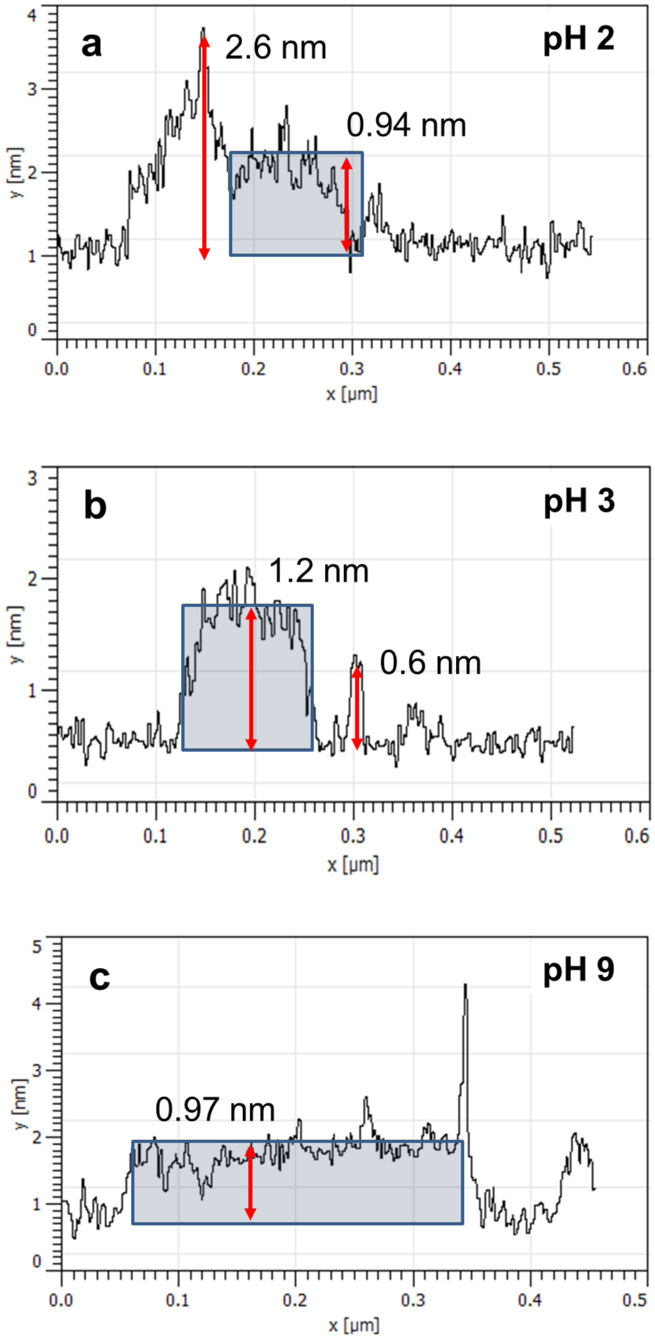

**Figure S7.** Height analysis in AFM images of pure gellan gum on mica indicates a decreasing thickness of gellan assemblies on the surface from >2 nm to ~1 nm upon increasing pH value (red arrows). The larger values correspond to multi-chain bundles and single chains are between 0.5 and ~1 nm height.

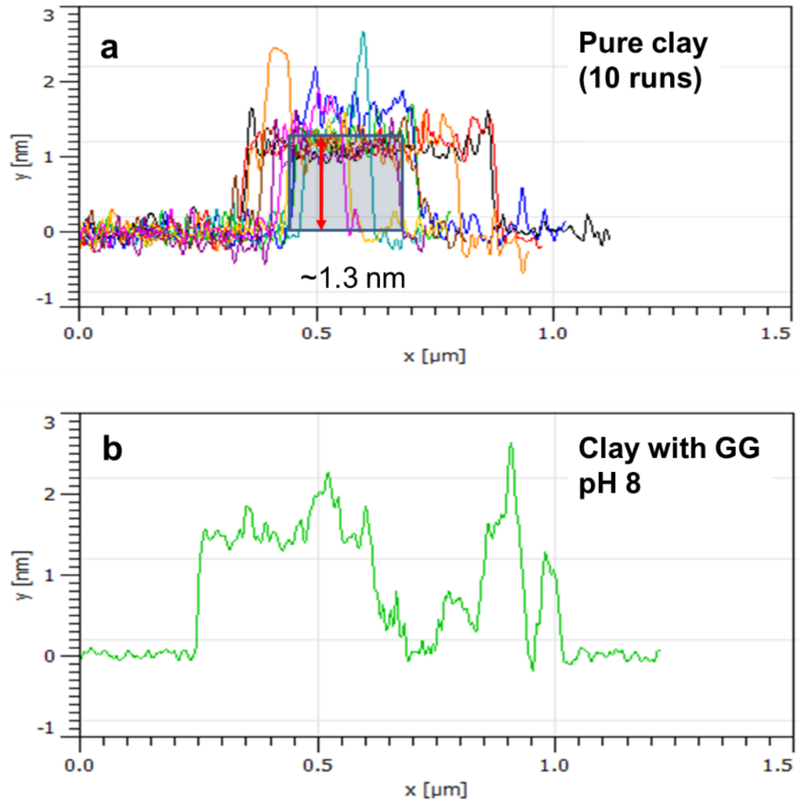

**Figure S8.** Height analysis in AFM images of (a) pure veegum clay on mica and (b) veegum clay with added gellan gum at pH 8. The resolution due to irregularity of the veegum clay platelets is not sufficient to distinguish bound gellan gum (GG).

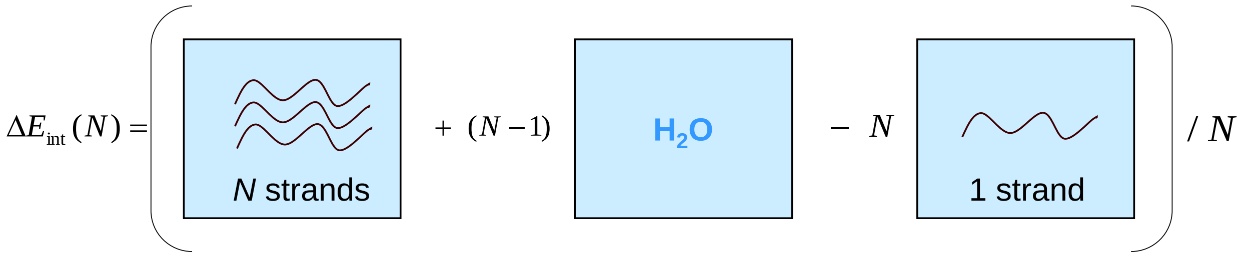

**Figure S9.** Method for the calculation of the interaction energy between the strands of gellan gum, normalized by the number of strands. Simulations of three systems in the NPT ensemble were carried out, and the average energies used to compute $\Delta E_{\text{int}}(N)$. $\Delta E_{\text{int}}(N)$ was further divided by the number of carbohydrate rings per strand to report a less length-dependent interaction energy.

**Table S1.** Composition of veegum clay minerals, models, and related clay minerals.

| Clay Mineral | Ref. | Formula | CEC [meq/100g] | | | | Description |
|---|---|---|---|---|---|---|---|
| | | | Exp. | Mono-valent[a] | Di-valent[a] | Total[a] | |
| Veegum clay minerals | | | | | | | |
| Veegum HV, Type IC | This study (Expt.) | $Na_{0.37}K_{0.03}Ca_{0.38}Mg_{0.05}[Si_4O_8][Al_{0.70}Fe^{III}_{0.04}Mg_{1.26}O_2(OH)_2]$ | NA | 104 | 198 | 302 | New laboratory measurements, $M_r$= 384.2 g/mol |
| Veegum | [2] (Expt) | $(Na_{0.371}K_{0.025}Ca_{0.384})[Si_4O_8][Al_{0.726}Fe^{III}_{0.045}Mg_{1.353}O_2(OH)_2]$ | 87 | 103 | 199 | 301 | Average formula for veegum clay |
| Regular veegum model | This study (Sim.) | $Na_{0.33}Ca_{0.435}[Si_4O_8][Al_{0.80}Mg_{1.20}O_2(OH)_2]$ | NA | 86 | 228 | 314 | Average stoichiometric veegum formula |
| Low Mg veegum model | [3] (Sim.) | $Na_{0.33}[Si_4O_8][Al_{1.67}Mg_{0.33}O_2(OH)_2]$ | 90 | 90 | 0 | 90 | Montmorillonite |
| High Mg veegum model | This study (Sim.) | $Na_{0.45}Ca_{0.48}[Si_4O_8][Al_{0.59}Mg_{1.41}O_2(OH)_2]$ | NA | 117 | 249 | 365 | Model with higher Mg content |
| Veegum model with leached MgO at edges | This study (Sim.) | $Na_{0.22}Ca_{0.33}[Si_4O_8][Al_{0.80}Mg_{0.88}O_{1.68}(OH)_{1.68}]$ | NA | 62 | 185 | 246 | Partially degraded veegum clay |
| Related clay minerals | | | | | | | |
| Montmorillonite (CEC can vary) | [3] | $(Na, K)_{0.321}[Si_4O_8][Al_{1.679}Mg_{0.321}O_2(OH)_2]$ | 87 | 87 | 0 | 87 | Possible proxy for Veegum |

| | | | | | | | |
|---|---|---|---|---|---|---|---|
| Hectorite | [4, 5] | $\sim Na_{0.35}[Si_4O_8][Mg_{2.65}Li_{0.35}O_2(OH)_2]$ | ~89 | 92 | 0 | 92 | Possible proxy for Veegum |
| Laponite | [6] | $\sim Na_{0.4}[Si_4O_8][Mg_{2.7}Li_{0.2}O_2(OH)_2]$ | 60-160 | 105 | 0 | 105 | $Mg^{2+}$ dissolution at pH <9, $SiO_2$ precipitation at pH 7-8 |
| Saponite | [4, 5] | $\sim Na_{0.3}Ca_{0.15}[Si_{3.4}Al_{0.6}O_8][Mg_{2.25}Fe^{II}_{0.75}O_2(OH)_2]$ | ~80 | 72 | 72 | 144 | Possible proxy for Veegum |

[a] Theoretical maximum of the cation exchange capacity if all interlayer cations would dissociate.

**Table S2.** Structure and conformation of gellan gum in dilute aqueous solution. Average shortest distances between individual strands and end-to-end distances, as well as the average shortest distance and end-to-end distance over all single, double, and triple strands at a given pH value, which reduces uncertainty. The distance between strands and the strand stiffness increase towards higher pH values. The model had a contour length of 25.7 nm and 48 carbohydrate rings.

| pH | System | Average shortest distance between strands (1-2), {1-3}, [2-3] (nm) | Average shortest distance between all strands (nm) | Root mean square end-to-end distance $r_{ee} = (<r^2>)^{1/2}$ (nm) | Average $r_{ee}$ over all strands (nm) |
|---|---|---|---|---|---|
| 2 | Single strand | NA | 0.7 ± 0.2 | 10.6 ± 0.7 | 8.4 ± 0.4 |
| | Double strands | (0.5) | | 5.6 ± 0.3 | |
| | Triple strands | (0.5), {1.3}, [0.6] | | 8.9 ± 0.5 | |
| 3.5 | Single strand | NA | 1.5 ± 0.3 | 10.3 ± 0.4 | 8.8 ± 0.4 |
| | Double strands | (1.0) | | 7.2 ± 0.3 | |
| | Triple strands | (1.5), {2.1}, [1.5] | | 8.9 ± 0.6 | |
| 9 | Single strand | NA | 2.2 ± 0.4 | 10.8 ± 0.6 | 10.5 ± 0.6 |
| | Double strands | (1.6) | | 12.5 ± 0.8 | |
| | Triple strands | (1.6), {2.3}, [3.2] | | 8.1 ± 0.5 | |

**Table S3.** Conformation of gellan gum single strands near the clay nanoplatelets in the simulation, measured by the average end-to-end length $r_{ee}$ for a contour length of 25.7 nm and 48 carbohydrate rings. The end-to-end lengths are shorter upon binding than they are in solution, indicating more conformational flexibility near all surfaces (except high Mg veegum where binding is not favored).

| pH | System | Root mean square end-to-end distance $r_{ee} = (<r^2>)^{1/2}$ (nm) |
|---|---|---|
| pH 3.5 | Regular veegum | 6.9 ± 0.3 |
| pH 9 | Regular veegum | 7.2 ± 0.4 |
| pH 3.5 | Regular veegum with 10 mM NaCl | 7.3 ± 0.5 |
| pH 9 | Regular veegum with 10 mM NaCl | 7.5 ± 0.4 |
| pH 3.5 | Low Mg veegum (montmorillonite) | 7.4 ± 0.5 |
| pH 3.5 | High Mg veegum (hypothetical composition) | 8.7 ± 0.5 |
| pH 3.5 | Veegum model with leached MgO at edges | 7.9 ± 0.4 |

## S1. Derivation of All-Atom Models for Veegum Clay

Veegum clay has been used in pharmaceutical formulations for decades, however, surprisingly the characterization remains very limited to-date.[2, 7-9] Veegum stabilizes emulsions and suspensions at low concentration and supports the reversible assembly of gels.[9]

We derived an average formula for veegum clay as $Na_{0.33}Ca_{0.435}[Si_4O_8][Al_{0.80}Mg_{1.20}O_2(OH)_2]$ with about ±5% uncertainty in the relative composition of Na, Ca, Mg and (Al + Fe) (Figure 1a-e). The composition is based on data by Lee, $(Na_{0.371}K_{0.025}Ca_{0.384})[Si_4O_8][Al_{0.726}Fe_{0.045}Mg_{1.353}O_2(OH)_2]$[2] and a new elemental analysis of veegum clay HV (Type IC), $Na_{0.37}K_{0.03}Ca_{0.38}Mg_{0.05}[Si_4O_8][Al_{0.70}Fe_{0.04}Mg_{1.26}O_2(OH)_2]$ (see Table S1 for all related compositions and models). A new elemental analysis (see methods) suggests a similar composition with minor differences. The structure is close to montmorillonite although it may be to some extent described as a hybrid of dioctahedral montmorillonite and trioctahedral Mg-rich saponite (Table S1), related to the occasional definition of veegum as a magnesium aluminum silicate obtained as a processed physical mixture (blend) of montmorillonite and saponite.[10] A remaining charge imbalance between the octahedral layer and the interlayer in Lee's model suggests that ~0.1 formula units of Mg would be present in the interlayer.[3, 11] The measured cation exchange capacity (CEC) of Lee's veegum of 87 meq/100g[2] suggests that most of the interlayer ions ($Ca^{2+}$, $Mg^{2+}$, $Na^{+}$, $K^{+}$) remain bound to the surface as otherwise the CEC would be about three times higher (the hypothetical maximum CEC is 301 meq/100g). The raw data on compositions were adjusted to balance the charge in the octahedral sheet versus the interlayer and to merge the Al and Fe(III) content as Al only for simplicity. Interlayer $Na^{+}$ and $K^{+}$ ions were both modeled as $Na^{+}$ ions, interlayer $Ca^{2+}$ and $Mg^{2+}$ were both modeled as $Ca^{2+}$ ions, and octahedral $Al^{3+}$ and $Fe^{3+}$ ions were both modeled as $Al^{3+}$ ions. This approximation is justified because of the amount of interlayer $K^+$, interlayer $Mg^{2+}$, and octahedral layer $Fe^{3+}$ ions are only a small percentage of majority ions with the same net charge. The actual CEC remains difficult to estimate from the formula and likely depends somewhat on the solution conditions, close to the reported value of 87 meq/100g[2] and much lower than the hypothetical maximum of 301 meq/100g upon dissociation of all monovalent and divalent cations.

The models and molecular dynamics simulations utilize IFF parameters for clay minerals similar to montmorillonite.[3, 12] IFF parameters describe chemical bonding (polarity), structures, surface, and hydration properties in high accuracy.[3, 12-14] We carefully assigned atomic charges to all atoms considering local chemical environments in analogy to existing clay models in the IFF model database (see atomistic models provided in the Electronic Supplementary Information).[12, 15-17] [11] The edge of each 5x5x1 $nm^2$ clay platelet contains 88 silanol groups. The groups were not ionized at pH 3.5, and 22 out of 88 silanol groups (25%) were ionized to sodium siloxide groups at pH 9.[17] The remaining edge atoms (AlOOH and $MgOOH^-$) carry atomic charges that correspond to electroneutral cleavage and introduce minimal local electric fields**.** We disregard the acid-base chemistry of the aluminol groups (AlOH) at the edges due to their much lower stoichiometric presence compared to SiOH groups (1:5). Partial protonation of (AlOH) to $Al(OH_2)^+$ groups below pH ~ 4 and partial dissociation to $AlO^- \cdots Na^+$ groups above pH ~ 4 can be included if needed.

Computed in-plane lattice parameters for regular veegum clay are the same as for montmorillonite within 1% and surface energies are reproduced as previously shown.[3] In aqueous solution, 15-20% of $Ca^{2+}$ and $Na^+$ interlayer ions dissociate more than 3 Å away from the surface atomic plane. The rest of the cations remains adsorbed on the clay mineral surface as seen in density profiles (Figure S2). Also, the migration of several $Ca^{2+}$ ions into the octahedral layer was observed during the simulation (Figure 1c), consistent with experimental observations by Lee and Vogt.[2, 7]

Additional all-atom models for veegum clay with lower and higher Mg content were represented by montmorillonite, a veegum clay with 17.5% increased Mg content, and by a model for an edge-leached veegum with 26% less Mg content (Table S1 and Figure S1). High Mg veegum may also be considered as a trioctahedral saponite, although high silicon and aluminum content likely promote a dioctahedral structure.

The model of the leached clay platelet, in particular, was derived to represent the possible influence of weathering and acidic environment. While always a small fraction of sodium ions exchanges for hydronium ions on the basal clay surface and elevates the pH value of the dispersion in water by a few units (Figures S1a), the leaching mechanism over time includes the dissociation of $Na^+$ ions and $Ca^{2+}$ ions from the surface of the clay platelet and removal of a stoichiometric amount of magnesium oxide hydroxide, MgO(OH) from the edges of the octahedral layer, effectively removing electroneutral units of $Na^+[MgO(OH)]^-$ (Figure S1b). To model this reaction, a bonded unit consisting of Mg, O, and an internal OH group in the octahedral layer was removed near the edge of the clay particle. The charge in the octahedral layer was increased by +1.0e as the MgO(OH) unit carries a net negative charge, and a single $Na^+$ ion (or half $Ca^{2+}$ ion) was removed atop the basal plane, changing the charge by -1.0e and the overall charge by ±0.0e. It was assumed that ~26% of Mg content (38/144 ions) leached out of the 5x5x1 $nm^3$ clay platelet. This amount corresponds to a drop in Mg content from 1.20 to 0.88 in the characteristic unit cell (Table S1 and Figure S1). We assumed that a mixture of sodium and calcium ions leaches, with some preference of sodium over calcium (sodium hydroxide being more soluble than $Ca(OH)_2$). The total change in surface charge on the 5 nm clay platelet due to leaching of 12 $Ca^{2+}$ and 14 $Na^{+}$ ions was ±38e. The final leached composition of clay platelet was 480 Si, 96 Al, 106 Mg, 40 Ca, and 26 Na.

## S2. The Shape of Clay Platelets

Grown clay platelets often show a preference for pseudo-hexagonal shape with more frequent occurrence of (010), (1-10), and (110) facets.[18] Common clay platelets, especially after grinding, typically have no regular shapes.[19, 20] This trend is also seen in the AFM images for veegum (Figure 3i, j) and can be explained by the arrangement of the atoms in the nanometer thick layers. The in-plane growth of clay platelets, or the in-plane cleavage, require the formation, or dissociation, of predominantly covalent Si-O-Si and Al-O-Al bonds (Figure S6). The internal orientation of these bonds appears to better facilitate row-by-row growth along the (010), (1-10), and (110) planes, and thereby explains preferences towards pseudo-hexagonal platelet shape observed by Nadeau.[18] (Figure S6c, d).[1] However, the number of chemical bonds per unit length is about the same along most (hkl) crystallographic planes, for example, including the vertical (100) planes, and therefore the cleavage energies along such (hkl) crystallographic planes are about the same as well (Figure S6c, d). As a result, cleavage occurs rather randomly along many different (h k l) crystallographic planes and leads to irregular shape (Figure S6c, d).

This rationale explains experimental data on platelet shape[18-20] and justifies the assumption of rectangular clay models consistent with AFM images (Figure 3j). The surface chemistry and local interaction of edge sites with polymers are very similar on all bounding (hkl) facets as all cleavage planes on the edges consist of SiOH and AlOH groups with pH dependent protonation/deprotonation equilibria, which are taken into consideration in our models. Recent simulations have also indicated minor changes in ion-edge interactions as a function of (hkl) facet,[21, 22] however, effects of variable pH values and changing ionization of the edge groups are much more significant and were not included in these models. Prior work on silica surfaces has shown that the amount of ionization of the silanol groups and the quantitative representation in models are much larger driving forces for interactions with ions and charged polymers than minor changes in surface topology or roughness,[17, 23] and similar effects are expected for the silanol and aluminol groups at clay edges.

## S3. Details of Computational Methods

**S3.1. Simulation Protocol.** The gellan and clay-gellan model systems were first subjected to 500 steps of energy minimization using the conjugate gradient algorithm to remove atomic close contacts during model building. Subsequently, all systems including multiple replicas were subjected to molecular dynamics simulation for a total simulation time of 100 ns using a time step of 1 fs. The TIP3P water model with rigid positions of hydrogen atoms relative to oxygen atoms helped accelerate the simulations. During the initial 90 ns, we employed the particle-mesh Ewald (PME) computation of electrostatic interactions with a low accuracy ($10^{-2}$) and a shortened spherical cutoff distance for pairwise Lennard-Jones interactions (8.5 Å) to reduce computation time for conformation sampling. Simulations during the last 10 ns runs were carried out with PME computation in high accuracy of $10^{-6}$ and a 12 Å cutoff for the Lennard-Jones interactions.

The entire trajectory was used to analyze chain conformations, average chain distances along the contour length and end-to-end lengths. The last 5 ns of the trajectory in high accuracy were employed to analyze equilibrium energies for each replica of the systems.

**S3.2. Ion Density Profile on the Clay Mineral Surfaces.** Simulation runs with the polymer away from the surface of the clay platelet were employed to compute the density profiles of the ions without interference from the polymer and its associated cations. Cation distributions on the surface of the clay platelet were recorded over the last 90 ns of simulation time using 90 snapshots (Figure S2). The shortest distance of each ion in the system from any of the atoms of the clay platelet was recorded to average over the 3D structure of the platelet.

**S3.3. Distance between Strands of Gellan Gum.** We chose 5 points along the chain contour of gellan gum and analyzed the distance distribution over the entire trajectory (Table S2). The reported distance is the average of the shortest distance between two polymer chains and the standard deviation.

**S3.4. End-to-End Distance, Persistence Length, and Radius of Gyration.** The average squared end-to-end distance $< r^2 >$ and the average end-to-end distance $r_{ee}$, approximated by the root mean squared end-to-end distance $(<r^2>)^{1/2}$, were obtained from several thousand instantaneous values throughout the simulation trajectory for each system (Figures 2 to 4, Tables S2 and S3). We use the average end-to-end distance as a relative measure of chain stiffness. As a more system-independent parameter, the persistence length $L_p$ could be computed from the mean squared end-to-end distance $< r^2 >$ and the total contour length $L = n \cdot l$ of the polymer with $n$ segments with a Kuhn length $l$ using the relationship for semiflexible and stiff polymer chains:[24]

$$< r^2 >= L \cdot L_p \left( 2 - \frac{l}{L_p} \right) - 2 \cdot L_P{}^2 \left( 1 - \frac{l}{L_p} \right) \left( 1 - e^{-\frac{L}{L_p}} \right). \qquad \text{(S1)}$$

However, the number of monomers that represent the Kuhn length $l$ is difficult to identify and the total contour length $L$ = 25.68 nm of the model chain with 48 carbohydrate rings is smaller than typical persistence lengths reported for gellan gum, which are on the order of 90 nm at 298 K and in a broader expected range of 10 to 150 nm for similar polysaccharides.[25] The radius of gyration can also be related to the persistence length $L_p$ via the contour length $L$:[24]

$$< r_g{}^2 > = \frac{L \cdot L_p}{3} - L_p{}^2 + \frac{2L_P{}^4}{L^2}\left(e^{-\frac{L}{L_p}} - 1\right) + \frac{2L_p{}^3}{L}, \tag{S2}$$

however, similar limitations in scale would apply.

**S3.5. Interaction Energy between Strands of Gellan Gum.** The interaction energy between the strands of gellan gum was computed using three separate NVT simulation boxes with interacting strands in water, water only, and an isolated strand in water (Figure S9). Thereby, $\Delta E_{\mathrm{int}}(N)$ is the interaction energy between strands of gellan gum normalized by the number of strands, and $\Delta E_{\mathrm{int}}(N)$ was further normalized by the number of carbohydrate rings per strand. The interaction energy between strands of gellan gum is thus reported per mol carbohydrate ring per strand (Figure 2g).

**S3.6. Binding Energy of Gellan Gum to Clay Platelets.** Binding energies of gellan gum to the clay platelets were obtained as a difference of the time-average energies of systems with the polymer in near ($E_{\mathrm{near}}$) and in the away ($E_{\mathrm{away}}$) configurations from the clay platelet (Figures 3 and 4). All systems were tested with up to five replicas for 100 ns each, and the average energies were corrected by the heat capacity of the systems for equal temperature of 298.15 K. The analysis involved visual inspection of the trajectories, interatomic distances, density profiles of cations, and end-to-end distances of the gellan chains (Table S3), aided by tools available in the VMD program.[26] The replicas of low energy were used to calculate the binding energy and the differences in the average energy between several replicas of the lowest energies are given as a measure of uncertainty. In addition, statistical fluctuations in block averages over tens of nanoseconds were utilized to assess uncertainties and in the same range.

**S3.7. Limitations and Uncertainties.** The simulations have been limited to model sizes between 10 and 20 nm. The contour length of the gellan chains of 25 nm and 48 carbohydrate rings in the models is short in comparison to gellan contour lengths of 100 nm to 1000 nm in experiments. Also, the clay platelets of ~5 nm size remain small in comparison to sizes of 10 nm to 1000 nm in experiments. Some influence also arises from the application of 3D periodic boundary conditions in the simulations, such as some residual interactions between periodic images of gellan gum and an influence on the reported conformations. The clay platelet has no interactions with periodic images due to the small size of 5 nm. Overall, the simulations present here provide the first insights into the dynamics of clay-gellan interfaces at a scale of ~10 nm in high resolution, including new models for veegum-type clays, while there are no current experimental techniques that could monitor such processes.

Simulation times of several 100 ns, aided by up to 10 replicas, provide generous insights into the dynamics and utilize the limits of current computational resources. It remains challenging to map out the equilibrium between all possible conformation states, however. Uncertainties in sampling are included in the given binding energies and in the conformation analysis. Future studies may capture larger systems, longer times, and higher accuracy to refine the reported mechanisms, adsorption energies, and trends in conformation preferences.

The quality of the force fields and computed molecular interactions is likely a small source of uncertainty. Further testing and possible refinements may benefit, in particular, predictions for long carbohydrate chains (>100 nm), and iterative feedback between simulations and measurements can guide improvements going forward.

## S4. Details of Elemental Analysis

The elemental analysis of Magnesium Aluminum Silicate HV (Type IC) included loss on dehydration (LOD), loss on ignition (LOI), X-ray diffraction, FT-IR measurements, and Scanning

Electron Microscopy (SEM). The average elemental composition by mass was Ca 10.8±0.9%, O 51.0±0.1%, Na 1.35±0.01%, Mg 11.2±0.2%, Al 6.76±0.07%, and Si 18.7±0.6% based on two independent measurements. The results agree within 1-3% with the earlier analysis by Lee et al and tend to be more accurate (Table S1).[2]

## Movie Captions

**Movie S1.** Dynamics of single strand gellan gum in aqueous solution at pH ~ 3.5 during 100 ns molecular dynamics simulation time.

**Movie S2.** Dynamics of double strand gellan gum in aqueous solution at pH ~ 3.5 during 100 ns molecular dynamics simulation time.

**Movie S3.** Dynamics of single strand gellan gum in aqueous solution at pH ~ 9 during 100 ns molecular dynamics simulation time.

**Movie S4.** Dynamics of double strand gellan gum in aqueous solution at pH ~ 9 during 100 ns molecular dynamics simulation time.

**Movie S5.** Dynamics of gellan gum in contact with low Mg veegum clay (montmorillonite) in aqueous solution at pH ~ 3.5 during 100 ns molecular dynamics simulation time. The polymer is attracted to the clay surface via ion-pairing with the help of cations (small blue spheres) in the interfacial electric triple layer and maintains contact with the edges of the clay platelet via hydrogen bonding for most of the time.

**Movie S6.** Dynamics of gellan gum in contact with regular veegum clay in aqueous solution at pH ~ 3.5 during 100 ns molecular dynamics simulation time. The polymer is attracted by ion pairing and maintains contact with the edges of the clay platelet via hydrogen bonding for part of the time.

**Movie S7.** Dynamics of gellan gum with high Mg veegum clay (hypothetical composition) in aqueous solution at pH ~ 3.5 during 100 ns molecular dynamics simulation. The polymer initially maintains contact with the edges of clay platelet via hydrogen bonding and one of the ends drifts over the basal surface. Gellan gum ultimately loses contact with the surface of the platelet and overall binding is unfavorable due to the high cation density and dense hydration layer.

**Movie S8.** Dynamics of gellan gum in contact with regular veegum clay in aqueous solution at pH ~ 9 during 40 ns molecular dynamics simulation time. The polymer is attracted to the clay surface by ion pairing and hydrogen bonding to edge groups is less prevalent. The higher degree of ionization of the polymer backbone and of the edge groups of the clay platelet at pH 9 leads to stronger binding and shifts contact away from the edges to the basal plane.

## Supplementary References

1. H. Heinz, *Clay Miner.*, 2012, **47**, 205-230.
2. K. P. Lee, *The Flocculation of Veegum Suspension by Electrolytes*, University of Utah, PhD Thesis, Salt Lake City, 1969.
3. H. Heinz, H. Koerner, K. L. Anderson, R. A. Vaia and B. L. Farmer, *Chem. Mater.*, 2005, **17**, 5658-5669.
4. W. Jaynes and J. Bigham, *Clays Clay Miner.*, 1986, **34**, 93.
5. R. V. Gaines, J. D. Dana and E. S. Dana, *Dana's New Mineralogy: The System of Mineralogy of James Dwight Dana and Edward Salisbury Dana*, Wiley, 1997.
6. D. W. Thompson and J. T. Butterworth, *J. Colloid Interface Sci.*, 1992, **151**, 236-243.
7. H. Vogt, *Die Pharmazeutische Industrie*, 1963, **25**, 12-15.
8. P. L. Kwang, C. M. Robert and T. Ree, *J. Korean Chem. Soc.*, 1972, **16**, 25-32.
9. *VEEGUM Magnesium Aluminum Silicate*, Vanderbilt Minerals LLC, Norwalk, CT, 2018.
10. Magnesium Aluminum Silicate, U. S. Pharmacopoeia, Rockville, MD, 2011, vol. NF 30, pp. 1845-1847.
11. H. Heinz and U. W. Suter, *J. Phys. Chem. B*, 2004, **108**, 18341-18352.
12. H. Heinz, T.-J. Lin, R. K. Mishra and F. S. Emami, *Langmuir*, 2013, **29**, 1754-1765.
13. R. K. Mishra, L. Fernández-Carrasco, R. J. Flatt and H. Heinz, *Dalton Trans.*, 2014, **43**, 10602-10616.
14. T. Z. Lin and H. Heinz, *J. Phys. Chem. C*, 2016, **120**, 4975-4992.
15. Y. T. Fu and H. Heinz, *Chem. Mater.*, 2010, **22**, 1595-1605.

16. G. D. Zartman, H. Liu, B. Akdim, R. Pachter and H. Heinz, *J. Phys. Chem. C*, 2010, **114**, 1763-1772.
17. F. S. Emami, V. Puddu, R. J. Berry, V. Varshney, S. V. Patwardhan, C. C. Perry and H. Heinz, *Chem. Mater.*, 2014, **26**, 2647-2658.
18. P. H. Nadeau, *Clay Miner.*, 1985, **20**, 499-514.
19. T. T. T. Ho, Y. S. Ko, T. Zimmermann, T. Geiger and W. Caseri, *J. Mater. Sci.*, 2012, **47**, 4370-4382.
20. R. H. A. Ras, Y. Umemura, C. T. Johnston, A. Yamagishi and R. A. Schoonheydt, *Phys. Chem. Chem. Phys.*, 2007, **9**, 918-932.
21. X. Liu, X. Lu, Y. Zhang, C. Zhang and R. Wang, *Phys. Chem. Chem. Phys.*, 2017, **19**, 18400-18406.
22. T. A. Ho, J. A. Greathous, A. S. Lee and L. J. Criscenti, *Langmuir*, 2018, **34**, 5926-5934.
23. F. S. Emami, V. Puddu, R. J. Berry, V. Varshney, S. V. Patwardhan, C. C. Perry and H. Heinz, *Chem. Mater.*, 2014, **26**, 5725–5734.
24. P. C. Hiemenz and T. P. Lodge, *Polymer Chemistry*, CRC press, 2007.
25. R. Takahashi, H. Tokunou, K. Kubota, E. Ogawa, T. Oida, T. Kawase and K. Nishinari, *Biomacromolecules*, 2004, **5**, 516-523.
26. W. Humphrey, A. Dalke and K. Schulten, *J. Mol. Graphics*, 1996, **14**, 33-38.